Why the September 2017 geomagnetic storm was stronger at certain locations than the famous Halloween event

M. Kellinsalmi[1,2], E. Marshalko[1], L. Juusola[1]and A. Viljanen[1]

[1]Finnish Meteorological Institute, Helsinki, Finland
[2]University of Helsinki, Helsinki, Finland

Key Points:

- This study compares the extreme geomagnetic storm of 2003 to the less intense but severe storm of September 2017
- The 2017 storm caused stronger magnetic variations at high latitudes in the Fennoscandian region
- Ionospheric current structures and ground conductivity gradients can produce intense localized magnetic field enhancements

Corresponding author: Mirjam Kellinsalmi, mirjam.kellinsalmi@fmi.fi

Abstract

In this study, we compare two significant geomagnetic storms of the 21st century: the well-known Halloween geomagnetic storm of 2003 (Kp index 9) and a somewhat milder storm of September 2017 (Kp 8). Both events caused exceptionally high values of geomagnetically induced currents (GIC) and earned a place among the top ten with respect to the measured GIC in the Finnish natural gas pipeline.. We analyze solar wind and geomagnetic data as well as modeled geoelectric fields during these two events to better understand the drivers behind these strong GIC. We discover certain geographic locations that experienced stronger magnetic field time derivatives during the 2017 storm. This is interesting because in terms of magnetic indices, the 2017 storm was a weaker event. We use equivalent currents to get a view of the ionospheric and induced currents in the Fennoscandian region. We find that the interplay between different structures of ionospheric currents and the three-dimensional ground conductivity leads to a complex behaviour of the geoelectric field. This study improves knowledge in space weather preparedness by identifying location-specific risks for geoelectric hazards, which can create severe problems in the high-voltage power grid.

Plain Language Summary

Intense solar eruptions, known as coronal mass ejections, can have major impact on the near-Earth space and cause geomagnetic storms. These events can cause problems to our satellites and even pose threat to high-voltage power grids on Earth. In this study we compare two major geomagnetic storms of the 21st century: the well-known Halloween event of 2003 and a slightly weaker storm of September 2017. We try to understand why certain geographic locations experienced stronger geomagnetic field variations during the 2017 storm, even though in general terms it was a weaker event. To achieve this, we use physical models to view the ionospheric currents and induced currents in the conducting ground in the Fennoscandian region. We find certain current structures in the ionosphere that can induce intense electric fields in the ground. Also, we discover specific geographic locations that are at a high risk for strong electric fields because they are located near areas with sharp variations in ground conductivity. This study improves knowledge in space weather preparedness by identifying location-specific risks for intense ground electric fields, which can create severe problems in high-voltage power grids.

1 Introduction

Severe geomagnetic storms can make the aurora glow at lower latitudes, but they can also cause unwanted effects such as disruptions in satellite-ground communications and global positioning systems as well as problems in high-voltage power networks. Strong storms can cause voltage fluctuations and damage transformers in electric grids. This is why geomagnetic storms are an important topic not only for space weather research, but also for civil aviation, military and power network operators. Because of these potentially significant issues, several countries, including Finland, have incorporated space weather awareness in their national risk assessment plans in recent years (Pulkkinen et al., 2017; *National risk assessment 2023*, 2023).

Coronal mass ejections (CMEs) are the primary drivers of the most intense magnetic storms, significantly amplifying both the speed of the solar wind and the strength of the magnetic field by several multiples when compared to quiet conditions. These sudden changes in the solar wind rattle the Earth's magnetic field causing ionospheric and magnetospheric currents. These, in combination with conducting properties of the ground, create a geoelectric field. The strength of the field is highly related to the ground conductivity. Conductivity refers to how easily charges can move through a material. In highly conductive materials (like salty sea water or graphite), charges can move more freely. This means that when an electric field is induced in the ground, the charges can redistribute

more easily, weakening the strength of the induced electric field. In regions with sharp contrasts in conductivity, these gradients cause charge accumulation which enhances the geoelectric field. This field drives geomagnetically induced currents (GIC) in ground-based conducting systems, such as high-voltage power grids and pipelines.

Measurements of the geoelectric field are sporadic and often very noisy. Consequently, the time derivative of the geomagnetic field ($d\mathbf{B}/dt$ and especially its horizontal part $d\mathbf{H}/dt$) is often used as a proxy because it is related to the electric field according to Faraday's law of induction:

$$\nabla \times \mathbf{E} = -\frac{\partial \mathbf{B}}{\partial t} \tag{1}$$

where $\mathbf{E}$ is the electric field, $\mathbf{B}$ is the magnetic field.

Magnetic field recordings are widely available for past events and in near real time, so it is handy to use them as GIC indicators. However, it is not possible to calculate GIC directly using the magnetic field or its time derivative. GIC can be calculated if the geoelectric field and parameters of a technological conductor are known. The geoelectric field can be modeled by coupling ground conductivity models with the measured magnetic field (for an extensive review, see Kelbert (2020)). In recent years, there has been a lot of progress in applying empirical magnetotelluric (MT) impedances (e.g., Bedrosian and Love (2015)) and using first-principle solutions with complex 3D conductivity models (e.g., Gao et al. (2021); Marshalko et al. (2021, 2023); Rosenqvist et al. (2022)). When the geoelectric field is known, calculation of GIC in power grids (Pirjola et al., 2022) or pipelines (Boteler, 2013) is a straightforward task.

As we have seen with past events, the strongest geomagnetic storms are clearly a key topic in considering GIC impacts on modern infrastructure. The best-known example is the Québec blackout in March 1989 affecting millions of people for several hours (Bolduc, 2002). A geographically more limited incident was the Malmö blackout in southern Sweden in October 2003 (Pulkkinen et al., 2005). Also worth mentioning is the May 1921 storm, which is comparable to the 1859 Carrington event. Although no direct recordings are available, GIC was strong enough to cause a destructive fire at a Swedish telephone station (Hapgood, 2019). This example gives a hint that a similar superstorm could have a serious impact on modern power grids.

As discussed above, the ground magnetic field has been a popular quantity in studying space weather events due to the good availability of data. Several recent studies (Schillings et al. (2022, 2023), Zou et al. (2022), Juusola, Viljanen, Dimmock, et al. (2023)) have gathered a lot of understanding of characteristics and different drivers of potentially significant GIC events. However, there is still a clear need to extend the analysis to the geoelectric field to have a more explicit connection to GIC. The ground conductivity plays a central role in terms of the internal contribution to the geoelectric field. In particular, ground conductivity distributions often have prominent 3D features with lateral gradients which lead to significant enhancement of the geoelectric field in their vicinity. It also follows that each region of interest requires a dedicated study due to the large variability in the ground conductivity (cf. Kelbert (2020); Love et al. (2022)).

In this study, we will compare two major geomagnetic storm: the Halloween event on 29-31 Oct 2003 and the event on 7-8 September 2017, to obtain deeper understanding of severe geomagnetic storms and related geoelectric field. The Halloween storm is one of the largest space weather events of which a lot of instrumental observations are available (Gopalswamy et al., 2005). It serves as a benchmark to other events thanks to good availability of different space weather data and many reported impacts on technology. The September 2017 event is one of the strongest storms of the previous solar cycle no. 24.

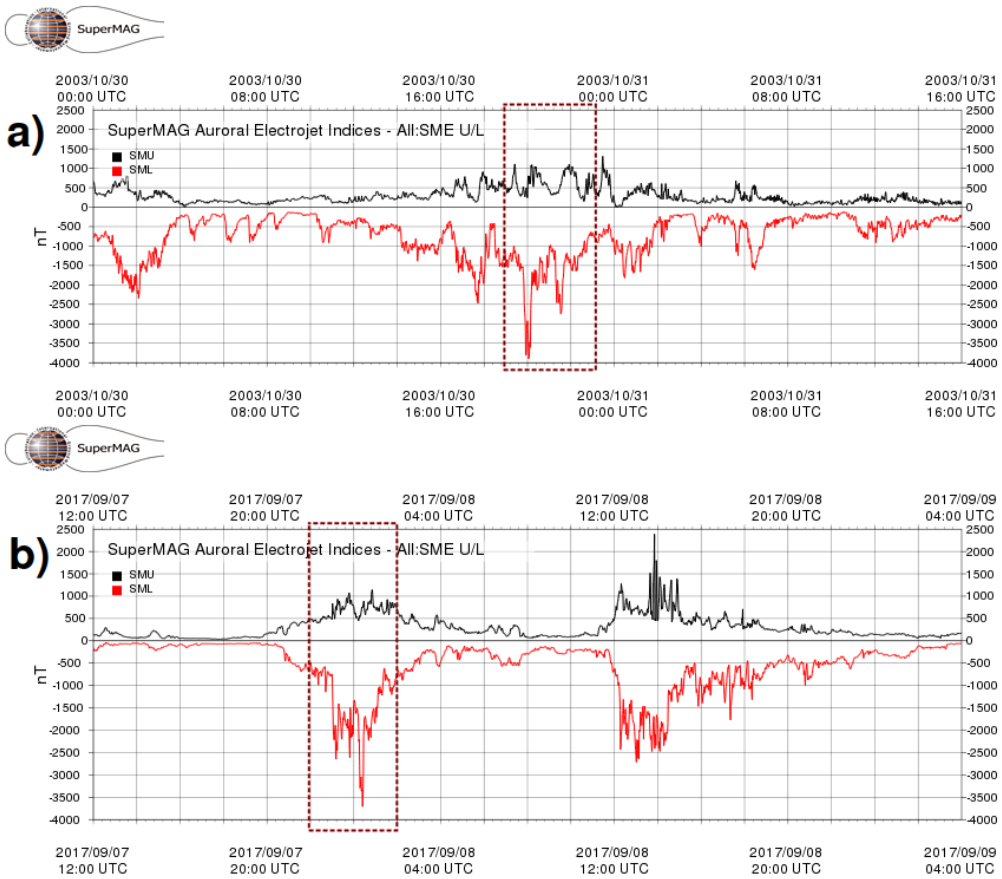

Figure 1. SuperMAG SMU and SML indices during two days of the Halloween geomagnetic storm (a) and two days of the September 2017 geomagnetic storm (b) (Gjerloev, 2012; Newell & Gjerloev, 2011). SMU is shown with black line and SML with red line. The dashed line boxes indicates the periods studied in this paper.

An important task is to find a meaningful way to compare events. Traditionally, magnetic storms are characterized by regional or global activity indices. However, many classical indices, such as Kp, have a limited range (index values 0-9) or are related to specific features of activity, such as the D_{st} index, which describes the magnetospheric ring current. Kappenman (2005) applied the method of morphology-based comparisons of interpolated and extrapolated ground magnetic field variations to illustrate significant differences between storms, which may look quite similar if only characterised by activity indices. We extend this idea with more quantitative analysis including the modeled geoelectric field.

2 Data and methods

2.1 Data

We use solar wind satellite observations from the OMNIWeb service (King & Papitashvili, 2020) for assessing the solar wind input to the magnetosphere. We use 10-s International Monitor for Auroral Geomagnetic Effects (IMAGE) magnetometer data, which is available via *IMAGE Magnetometer network* (2023). We also use magnetic indices, like Kp, SML and SMU. The Kp index is based on magnetic measurements at mid-

latitudes and shows the range of horizontal magnetic field variations during a 3-hr period. We use the Potsdam Kp index as defined by Matzka et al. (2021). The SuperMag SML and SMU indices describe the maximum westward and eastward auroral electrojets' strength, respectively. SMU is the upper, and SML is the lower envelope of the north component for stations between 40° and 80° magnetic north (Newell & Gjerloev, 2011). Figure 1 shows the values of the SML/U indices during both storms. Other relevant indices are IU and IL. They are similar to SML/U but use data from the IMAGE network, which is a localized subset of the SuperMag network.

During both storms, we focus on 4-hr periods when clear substorms are visible in the magnetograms (see Fig. 2).

- For the Halloween event the chosen period is: 2003-10-30 19:00 to 23:00 UT
- For the September 2017 event: 2017-09-07 22:00 UT to 2017-09-08 02:00 UT

2.1.1 Halloween event

The Halloween event was caused by a series of strong, X-class flares accompanied by several CMEs on the Earth-facing side of the Sun. The event caused hours long outages in spacecraft measuring solar wind, and many data sets from this period are uncertain or have long data gaps. In fact, approximately half of the Earth's satellites experienced some problems due to these eruptions (Phillips, 2021). It is estimated that the CMEs could have had a velocity of over 2200 km s^{-1} (Skoug et al., 2004). This is approximately 5 to 6 times higher than during typical slow solar wind conditions, when solar wind speed ranges between 300 and 400 km s^{-1}.

These CMEs caused the strongest magnetic storm of the past few decades. The Potsdam Kp index reached 9 (extreme) for two consecutive 3-hr periods and D_{st} reached -400 (Skoug et al., 2004). The SML index peaked at -3600 nT, and IL index at -4500 nT during the studied period. SML/U indices during the Halloween event are shown in Figure 1 (a), where the studied period is highlighted. The magnetic north component (X-component) measurements during the studied period are shown in Figure 2, left panel. These magnetograms show that there were intense variations observed at all of the shown magnetometer stations. Record-large GIC, up to 57 A, were measured in the Finnish natural gas pipeline during the Halloween storm (Tsurutani, Bruce T. & Hajra, Rajkumar, 2021; Dimmock et al., 2019) at 2003-10-29 06:57 UT. The blackout in Malmö (55.6° N) started on 30 October at 20:07:15 UT (Pulkkinen et al., 2005, Table 2).

2.1.2 September 2017 event

The origin of the 2017 event was, as well, a series of moderate to strong (M to X-class) solar flares associated with several CMEs. The solar wind speed was measured to be up to 800 km s^{-1}. The CMEs caused severe geomagnetic disturbances with Kp-index between 7 to 8 (strong to severe) and D_{st} -150 (Dimmock et al., 2019). The SML index peaked at -3700 nT, and SMU at 1100 nT. SML/U indices during the September event are shown in Figure 1 (b), where the studied period is highlighted.

SML/U values are similar to those of the Halloween event, but the number of stations is also higher in 2017 compared to 2003. This is why these indices are not directly comparable. Regarding the Kp and D_{st}-index, this was clearly a weaker storm, but we still observed very high GIC values (30.1 A at 00:31 UT, 8 September 2017) at the Mäntsälä station in Finland (Dimmock et al., 2019). This event made it to the top 10 of highest measured GIC at Mäntsälä. However, we also note that GIC values of different years are not fully comparable due to gradual changes in the pipeline network.

Although no major power failures are associated with the storm, at 00:29 UT on 8 September 2017, a transformer tripped near Sundsvall, central Sweden (Rosenqvist et

Station	Geo. Lat. [° N]	Geo. Lon. [°E]	CGM Lat. [° N]	CGM Lon.[°E]
Sørøya (SOR)	70.54	22.22	67.34	106.17
Kevo (KEV)	69.76	27.01	66.32	109.24
Ivalo (IVA)	68.56	27.29	65.10	108.57
Muonio (MUO)	68.02	23.53	64.72	105.22
Sodankylä (SOD)	67.37	26.63	63.92	107.26
Pello (PEL)	66.90	24.08	63.55	104.92
Oulujärvi (OUJ)	64.52	27.23	60.99	106.14
Hankasalmi (HAN)	62.25	26.60	58.69	104.54
Nurmijärvi (NUR)	60.50	24.65	56.89	102.18
Tartu (TAR)	58.26	26.46	54.47	102.89

Table 1. Geographic and corrected geomagnetic (CGM, 2001) coordinates of the magnetometer stations mentioned in this study.

al., 2022). Sundsvall is located at a similar latitude as Hankasalmi (HAN) station. Effects were also seen in the southern hemisphere. A station in southern New Zealand reported enhanced GIC levels on 7-8 September 2017 (Clilverd et al., 2018). At high latitude magnetometer stations in Fennoscandia, we saw larger time derivative values of the horizontal magnetic field, d$\mathbf{H}$/dt, than during the Halloween event. The magnetic north component (X-component) measurements during the studied period are shown in Figure 2, right panel. These magnetograms show that the most intense variations were observed north of Nurmijärvi (NUR).

The original reason for studying the Halloween and 2017 storms specifically, was an observation that the maximum values of d$\mathbf{B}$/dt of the September 2017 event exceeded those of the Halloween storm at high latitudes of the Fennoscandian mainland. This raises the question of why the September 2017 event did not reach or exceed the magnitude of the Halloween storm elsewhere.

2.2 Methods

We utilize solar wind measurements, ground-based magnetometer data, and results of 3D geoelectric field modeling. We focus on Fennoscandia, where an extensive coverage of ground-based magnetometer data of both events (Dimmock et al., 2019; Juusola, Viljanen, Dimmock, et al., 2023) and detailed ground conductivity models are available (Korja et al., 2002). Using 3D induction simulations, we have a controlled physical model providing the geoelectric field related to geomagnetic variations. We analyse magnetic field variations, their time derivatives, and the geoelectric field to obtain a comprehensive view of the events from the GIC perspective. We apply methods similar to Juusola, Viljanen, Dimmock, et al. (2023) but as an addition, include the modeled geoelectric field.

The Halloween and the September 2017 events are first compared by simply taking the ratio of the highest values for measured d$\mathbf{H}$/dt and modeled horizontal geoelectric field. The time derivative of the horizontal geomagnetic field, $\mathbf{H}$, is given by:

$$\mathrm{d}\mathbf{H}/\mathrm{d}t = \frac{\mathrm{d}B_x}{\mathrm{d}t}\hat{\mathbf{e}}_x + \frac{\mathrm{d}B_y}{\mathrm{d}t}\hat{\mathbf{e}}_y \tag{2}$$

where B_x is the northward and B_y is the eastward component of the geomagnetic field. We also show plots utilizing the 2D Spherical Elementary Current System (SECS) method, described by Vanhamäki and Juusola (2020). With this method, we can calculate the

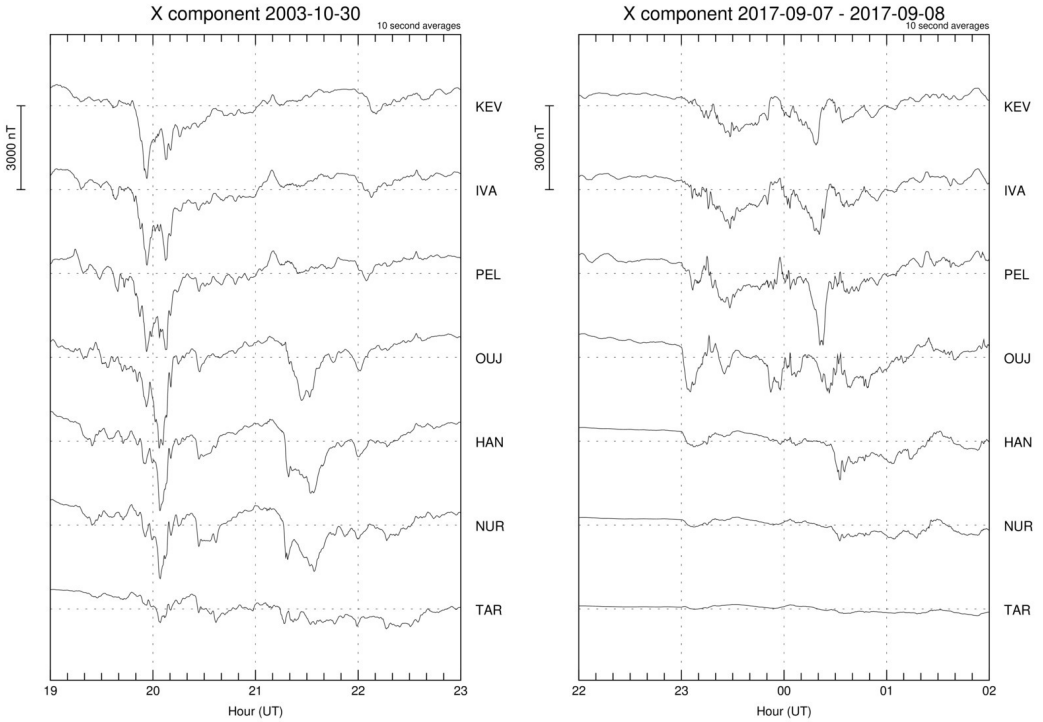

Figure 2. Measured geomagnetic north component (X-component) at seven magnetometer stations during 4 hr of the Halloween event (left panel) and the 2017 storm (right panel). In the 2003 storm we see a dip of almost 4000 nT in the X-component of Oulujärvi (OUJ) station. Also, Tartu (TAR) station shows moderate disturbances. In the case of the 2017 storm, we see a dip of over 2000 nT at Pello station (PEL), but very limited effects in Tartu (TAR) station. Figures retrieved from *IMAGE Magnetometer network* (2023).

equivalent external (ionospheric) and internal (telluric) currents and the corresponding ground magnetic field.

The horizontal geoelectric field, $\mathbf{E}_h$, is given by:

$$\mathbf{E}_h = E_x \hat{\mathbf{e}}_x + E_y \hat{\mathbf{e}}_y \tag{3}$$

where E_x and E_y are the north- and eastward components of the geoelectric field, respectively.

It is convenient to use the local plane wave approximation, which implies that the source of the electromagnetic induction is locally spatially uniform, for the geoelectric field calculation at IMAGE magnetometers' locations. Plane wave assumption allows researchers to relate the surface horizontal frequency-domain geoelectric field with the surface horizontal frequency-domain magnetic field at point $\mathbf{r}$ through an MT impedance (Berdichevsky & Dmitriev, 2008)

$$\mathbf{E}_h^{pw}(\mathbf{r},\omega) = \frac{1}{\mu_0} Z(\mathbf{r},\omega)\mathbf{H}^{pw}(\mathbf{r},\omega), \quad Z(\mathbf{r},\omega) = \begin{pmatrix} Z_{xx} & Z_{xy} \\ Z_{yx} & Z_{yy} \end{pmatrix}, \tag{4}$$

where μ_0 is the magnetic permeability of free space.

Note that even though in reality the source of the ground electromagnetic field is always laterally variable, previous studies (Marshalko et al., 2021, 2023) demonstrated that 3-D electromagnetic modeling in combination with the local plane wave approximation produces reasonable geoelectric field in the Fennoscandian region.

The geoelectric field in this paper is simulated as follows:

1. 3D electromagnetic forward modeling is carried out via PGIEM2G code with two (laterally uniform) plane wave sources for the SMAP (Korja et al., 2002) conductivity model (the variant of the model which was previously used by Marshalko et al. (2021, 2023); Kruglyakov et al. (2022, 2023)) and an underlying 1D conductivity profile from Kuvshinov et al. (2021) at fast Fourier Transform (FFT) frequencies ranging between $\frac{1}{L}$ and $\frac{1}{2\Delta t}$, where L is the length of the (input) magnetic field time series and Δt is the sampling rate of this time series. 3D MT impedances $Z(\mathbf{r},\omega)$ are then calculated for each FFT frequency ω.
2. Time-varying horizontal magnetic field $\mathbf{H}^{obs}(\mathbf{r},t)$ observed by magnetometers is converted from the time to frequency domain using FFT.
3. Further, the horizontal geoelectric field is calculated for each frequency and each magnetometer $\mathbf{r}$ as
$$\tilde{\mathbf{E}}_h^{pw}(\mathbf{r},\omega) = \frac{1}{\mu_0} Z(\mathbf{r},\omega)\mathbf{H}^{obs}(\mathbf{r},\omega). \tag{5}$$
4. Finally, an inverse FFT is performed for the frequency-domain geoelectric field to obtain the geoelectric field in the time domain.

Note that in order to avoid an artificial amplification of the geoelectric field at the ends of 4-hr time intervals due to the so-called Gibbs effect, we perform geoelectric field calculation for $L = 8$ hr time intervals (2003-10-30 17:00 - 2003-10-31 01:00 UT, 2017-09-07 20:00 - 2017-09-08 - 04:00 UT). The sampling rate of the input magnetic field time series is $\Delta t = 10$ s.

Usefulness of the modeled geoelectric field is highly dependent on the ground conductivity, which is not perfectly known. This leads to a considerable uncertainty of the geoelectric field amplitudes, which can vary a lot in short (tens of kilometers) length scales (Marshalko et al., 2023), whereas the magnetic field changes much less. A possible way

Parameter	Halloween event	2017 event
Solar wind speed [km/s]	2240	820
Kp	9	8
D_{st}	-383	-150
GIC [A]	57.0	30.1
Boundary [° MLAT]	49.4	55.8

Table 2. Geomagnetic and solar wind indices and approximate location of the auroral oval boundary during the peak of the Halloween and the September 2017 geomagnetic storms. Values retrieved from King and Papitashvili (2020), Skoug et al. (2004), Matzka et al. (2021), Hajra et al. (2020).

to circumvent this issue is to use relative values, i.e., to perform a comparison with respect to a benchmark event.

To get a visually convenient time series plots of d$\mathbf{H}$/dt and the electric field, normalization of data for each station was carried out in the following way:

$$f_n(t) = \frac{|f(t)|}{\max(|f(T)|)}, \tag{6}$$

where $f(t)$ is a single value of the time series f (e.g. the horizontal geoelectric field, $\mathbf{E}_h$) at time t, $f_n(t)$ is the corresponding normalized value, and $\max(|f(T)|)$ is the maximum value of the whole 4-hr period at a specific station.

One more measure of the strength of a magnetic storm is the extent of the auroral oval. This region is located near the border of the open and closed magnetospheric field lines, and gets the most intense particle precipitation from the magnetosphere. There have been studies, e.g. Xiong et al. (2014) and Blake et al. (2021), that provide estimates of the oval boundaries as a function of the D_{st}-index. Blake et al. (2021) states that the equatorward boundary of the oval is given by:

$$\text{Boundary(MLAT)} = 36.7 - \frac{9400}{D_{st} - 342}, \tag{7}$$

where MLAT is the magnetic latitude, and this applies for condition $-1150 < D_{st} < 0$ nT.

Maximum values of some indices and parameters of the two storms obtained based on solar wind data from OMNIweb (King & Papitashvili, 2020), estimates from Skoug et al. (2004) and the equation above are listed in the Table 2.

3 Results

Figure 3 shows the comparison of the largest values of the measured d$\mathbf{H}$/dt and the modeled horizontal geoelectric field. We see that for higher latitudes both ratios ($\mathbf{E}_h$ and d$\mathbf{H}$/dt) are larger. The ascending trend is clear for d$\mathbf{H}$/dt, but a bit less obvious for $\mathbf{E}_h$. For example, at Kilpisjärvi station (KIL), the ratio of d$\mathbf{H}$/dt is greater than 1 and the ratio of $\mathbf{E}_h$ is slightly less than 1, meaning that at KIL the 2017 event was actually stronger with respect to the measured magnetic field time derivative and almost similar with respect to the magnitude of $\mathbf{E}_h$. Generally ratios of d$\mathbf{H}$/dt are larger than those of $\mathbf{E}_h$, and the stations Muonio (MUO) and Søroya (SOR) clearly stand out with

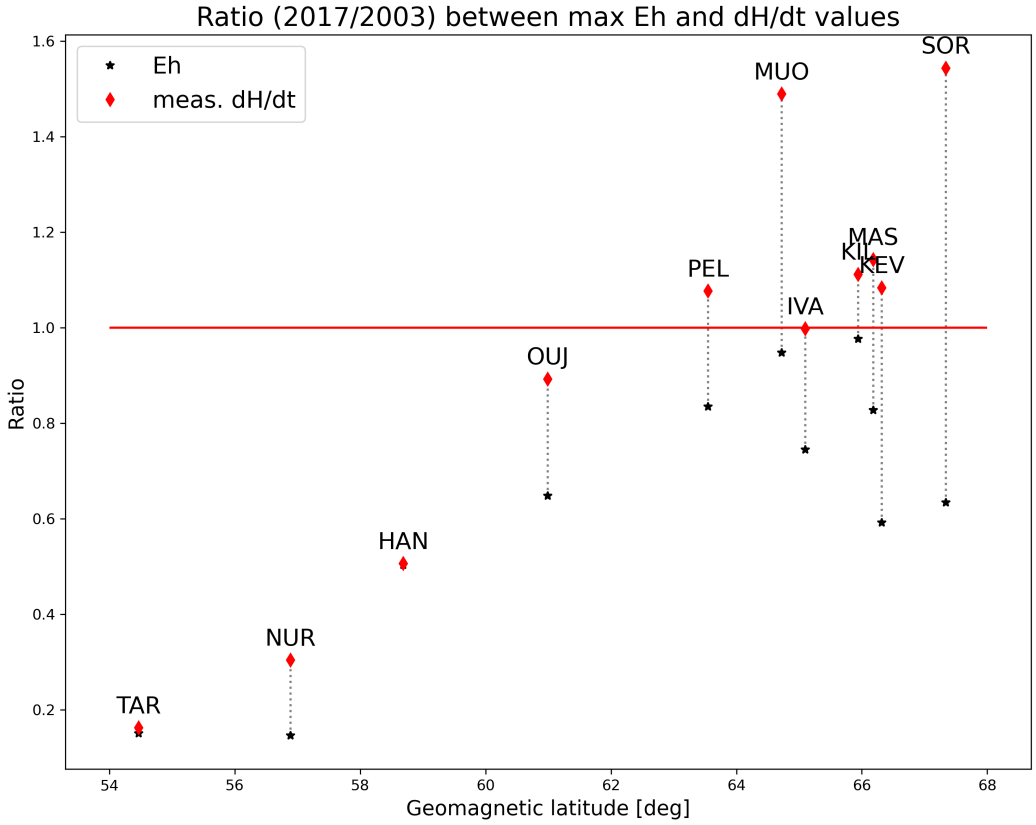

Figure 3. Ratio of the maximum values of the modeled horizontal geoelectric field, $\mathbf{E}_h$ (black stars), and measured d$\mathbf{H}$/dt (red diamonds) during the studied periods of the Halloween and September 2017 events. Ratios are shown as functions of the geomagnetic latitude (CGM for year 2001). The red line emphasises ratio equal to unity, i.e. the same magnitude for both events. For visual clarity, black stars and red diamonds corresponding to a specific station are connected by a dotted line.

their maximum d$\mathbf{H}$/dt values. Another interesting feature is the descending ratios of $\mathbf{E}_h$ at latitudes higher than MUO station (CGM latitude 64.7 °).

Figure 4 (a) and (b) show normalized values of the magnitude of the horizontal geoelectric field at 11 stations. In this plot, we can easily see if the peaks in the horizontal geoelectric field ($\mathbf{E}_h$) occur at the same times at different locations. For the Halloween storm (a), we see that the peak values for all stations are concentrated at around 20:00 UT ± 10 min. There is also a secondary peak at HAN, NUR, and TAR stations at 21:20 UT which is not so clearly visible in the northern stations. In the case of the 2017 storm (b), we see that the $\mathbf{E}_h$ enhancements are more spread out between 23:00 UT and 00:30 UT. Stations OUJ, HAN and TAR show a sharp rise in $\mathbf{E}_h$ at 23:00, but this is not visible at other stations. In a similar way, Figure 4 (c) and (d) show the normalized values of the measured horizontal magnetic field time derivative. Maximum value for each station is marked with a red triangle marker. The behavior of d$\mathbf{H}$/dt is quite similar to that of $\mathbf{E}_h$. The peak values at different stations are more concentrated in the 2003 event than in the 2017 event. In the next few figures, we focus on the exact moments of these most intense values and use equivalent currents to visualize the ionospheric and induced parts of the horizontal magnetic field and currents.

Figure 5 shows the temporal development of different magnetic field parameters. Figures 6-9 demonstrate ionospheric and telluric currents and external/internal magnetic fields in the Fennoscandian region. All the figures show, side by side, the 2003 and 2017 events at the moment of maximum amplification of each quantity (d$\mathbf{H}$/dt, $\mathbf{E}_h$) at Muonio (MUO) station for comparison. MUO was one of the stations where the 2017 storm caused a significantly stronger d$\mathbf{H}$/dt than the Halloween event (see Figure 4 (c),(d)).

Figure 6 shows snapshots of the time derivatives of external currents and horizontal magnetic field at MUO station, for both events, at moments of maximum d$\mathbf{H}$/dt. In the right panel (2017 storm), we see that there is a strong local intensification of the external current, d$\mathbf{J}$/dt, to the west of MUO station. In terms of intensity, this is about twice as strong as during the Halloween event. Maximum values are shown in the text box in the top left corner of each plot. During the Halloween event, the time derivative of the external current shows intensification in a much wider area south of MUO. Similarly, with the internal current in Figure 7 (right panel), we see a very localized pattern around MUO, PEL and SOD stations, with strong values of the internal d$\mathbf{H}$/dt.

Figure 8 shows snapshots of the time derivatives of the external currents and horizontal magnetic field at MUO station, during both of the studied storm periods, at moments of maximum $\mathbf{E}_h$. The horizontal geoelectric field values at MUO station were slightly weaker during the 2017 event. In Figure 8, we see quite similar patterns between the 2003 and 2017 events. The strongest enhancement in the external d$\mathbf{H}$/dt is seen approximately between MUO and RAN stations. Figure 9 shows plots of the internal d$\mathbf{J}$/dt and d$\mathbf{H}$/dt. There we see again a very localized enhancement near Kevo (KEV) station during the Halloween event (left panel). During the 2017 snapshot (right panel) the internal currents have quite a complex structure, with one clear hot spot near KIL station.

Finally, we briefly look at the approximate location of the auroral oval during these two storms. The latitudinal range of the auroral oval also increases with stronger geomagnetic activity. According to Xiong et al. (2014), the quiet time ($K_p = 1-2$) range of the oval is a little less than 10°. During geomagnetic storms ($K_p > 4$), the extent of the oval is up to 15° in latitude. Based on these estimates, during the studied 4-hr period, the oval was, on average, located between 54 and 69°N MLAT during the Halloween event, and between 60 and 75°N in MLAT during the 2017 storm. During the Halloween event, the auroral oval was about 6° closer to the equator than during the September 2017 event.

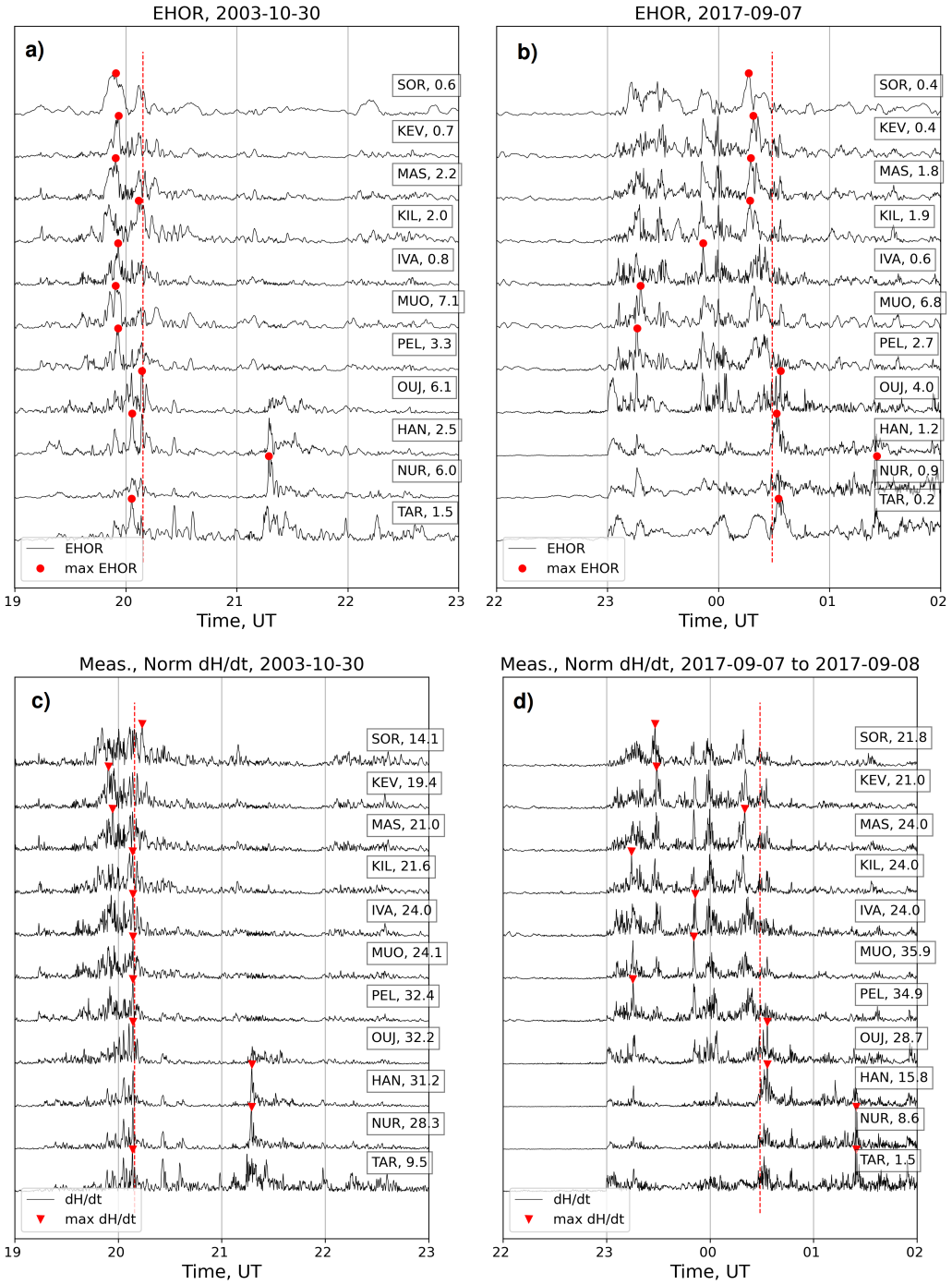

Figure 4. Normalized values of the modeled $\mathbf{E}_h$ (a),(b) and measured d$\mathbf{H}$/dt (c),(d) magnitude for 11 stations organized by descending geomagnetic latitude. The left panel shows a 4-hr period of the Halloween event and the right side 4 hr of the September 2017 event. The red markers show the time at which the the maximum value occurred. The vertical red dashed line shows the time of the Malmö blackout during the Halloween event and the power transformer issues reported during the September 2017 storm near Sundsvall, Sweden. The stations' name abbreviations are shown in text boxes on the right in each plot. The text box also shows the maximum value [V/km] in (a),(b) and nT/s in (c),(d) for each station.

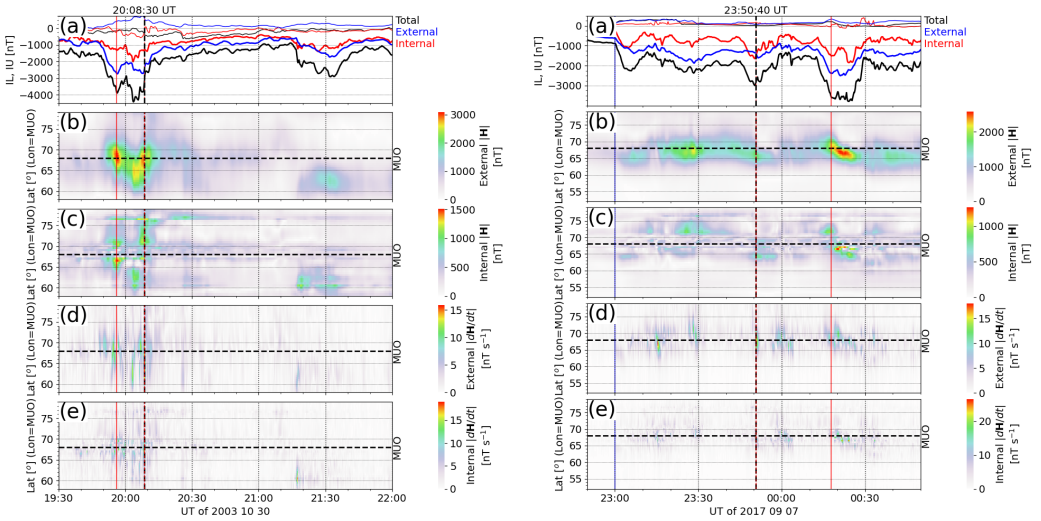

Figure 5. Keograms of the magnetic field strength during the Halloween event (left) and September 2017 event (right). The panels show the temporal development of different magnetic field parameters. Panels from the top are the IL/IU indices, absolute magnitude of the external/internal horizontal magnetic field and its time derivative. The dashed horizontal line marks the latitude of MUO (Muonio) station, and the vertical lines indicate its highest $\mathbf{E}_h$ (red line) and measured d$\mathbf{H}$/dt value (black dashed line). The blue vertical line in the right panel indicates the sudden storm commencement.

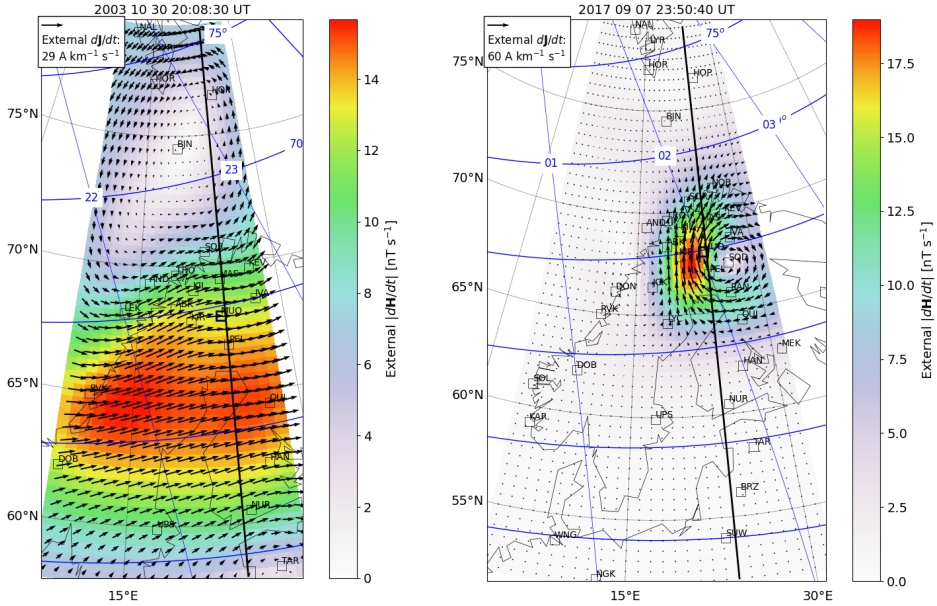

Figure 6. Time derivatives of the ionospheric (external) equivalent current density and the external part of the ground magnetic field calculated by fitting the measured magnetic field with two layers of SECSs at 90 km altitude and 1 m depth. Similar plots are shown for the Halloween event (left, 20:08:30 UT, 30 October 2003) and the 2017 event (right, 23:50:40 UT, 7 September 2017). The shown time is the moment of maximum measured d$\mathbf{H}$/dt at MUO station.

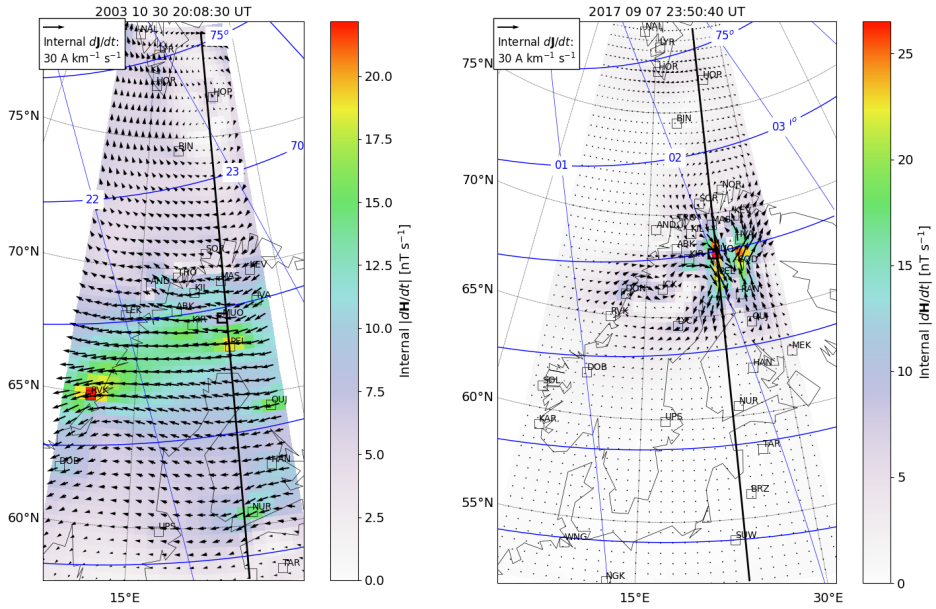

Figure 7. The same as Figure 6 except that the arrows show the time derivative of the induced (internal) equivalent current density instead of the ionospheric equivalent current density and the color scale shows the time derivative of the internal part of the horizontal ground magnetic field.

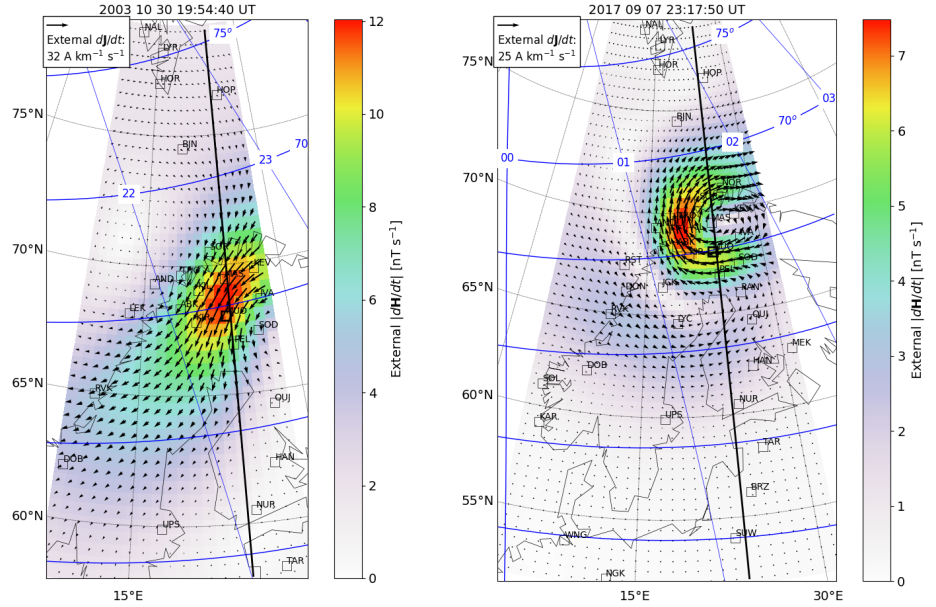

Figure 8. The same as Figure 6 except for the time of the $\mathbf{E}_h$ peak at MUO instead of the time of the d$\mathbf{H}$/dt peak.

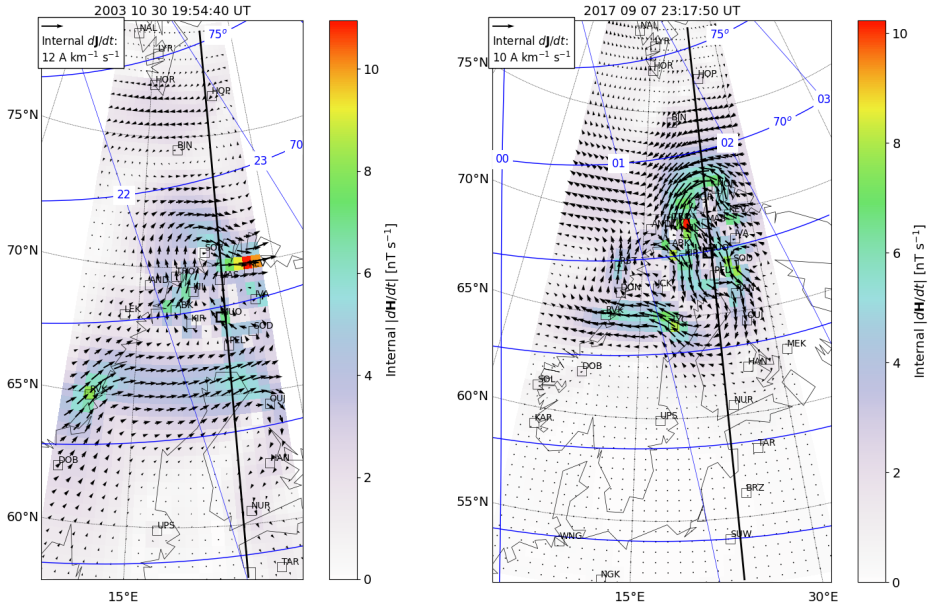

Figure 9. The same as Figure 7 except for the time of the $\mathbf{E}_h$ peak at MUO instead of the time of the d**H**/dt peak.

4 Discussion

In this study, we compared 4-hr periods of the extreme Halloween storm and the severe September 2017 storm. With regards to solar wind parameters and magnetic indices, the Halloween event was clearly stronger. However, comparison of the ground based magnetometer measurements shows that the 2017 storm was stronger at high latitudes and produced very high GICs. We observed station-specific enhancements in the electric and magnetic field magnitudes, and we used equivalent currents and ground conductivity mapping to help explain the ionospheric and telluric sources for these very localized enhancements. We start the discussion with the ionospheric sources.

The latitudinal extension of the auroral oval is related to the strength of magnetospheric disturbance. Based on estimates of Blake et al. (2021) and Table 2, we conclude that the auroral oval was around 6 degrees lower in latitude during the Halloween storm. Also, in Figure 5 (left panel, second plot from the top) we see that the enhancement of the external **H** during the Halloween storm begins in the north (north of MUO station) and then moves equatorward (from 70 to 60° N) during the next tens of minutes. In Figure 5 (right panel, second plot from top) we see that the enhancement during the 2017 storm remains at high latitude, between 65 to 70° N. These observations indicate that the strongest ionospheric currents during the Halloween storm were located south of the stations where we saw the largest d**H**/dt values in the 2017 storm.

Another observation we made regarding the latitudinal differences is related to Figure 3. There was a clear ascending trend in the ratios of the parameters up until MUO station (CGM latitude 64.7°), meaning that with increasing latitude, the ratios of d**H**/dt and $\mathbf{E}_h$ seemed to grow stronger in favour of the 2017 event. This is expected since the large-scale ionospheric currents were located at higher latitudes in the 2017 event. At stations IVA, MAS, KEV, and SOR something more complicated happens. The ratios of the two parameters start to drift apart, so that d**H**/dt keeps increasing but $\mathbf{E}_h$ begins to decrease. In other words, the geoelectric field at high latitudes, at most stations,

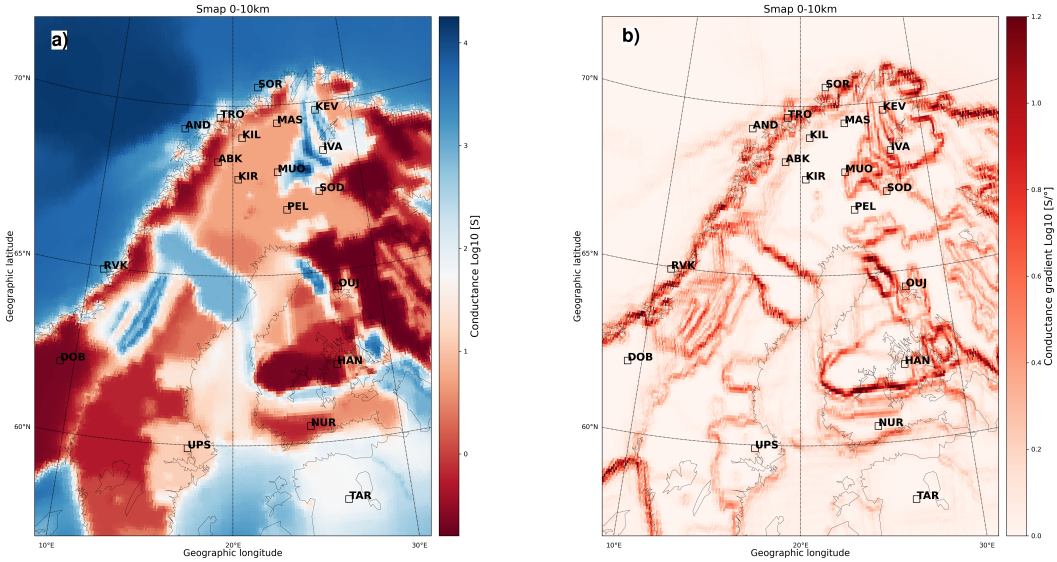

Figure 10. (a) Ground conductance based on SMAP 0-10 km data (Korja et al., 2002). Conductance is higher in the sea but also in some land areas, like the Finnish Lapland. A few IMAGE station locations and name abbreviations are marked on the map. (b) Horizontal gradient of the ground conductance based on SMAP 0-10 km data. Sharp gradients are visible along the Norwegian coastline but also inland. Several Finnish stations, e.g. SOD, MUO and KEV, are located on top of strong horizontal conductance gradients.

is weaker during the 2017 event, even though it has a stronger ionospheric driver. The explanation may be related to the conductivity structures of the ground and the orientation of the ionospheric currents.

The geoelectric field is enhanced or weakened depending on the orientation of the ground conductivity gradients in relation to the ionospheric currents. The stations SOR, KEV, and MUO, which stood out in the Figure 3, are located near areas of high conductivity or quite sharp conductivity gradients. Figure 10 demonstrates the distribution of conductance (depth-integrated conductivity) and the horizontal conductance gradient in the upper layer of the SMAP model. Different kind of behavior of the geoelectric field at stations SOR and KEV is probably related to the higher ground conductivity which is able to dissipate the charges quicker. This weakens the geoelectric field in the region. The case of MUO station is a bit different. The behavior of $\mathbf{E}_h$ at this location can be related to the nearby sharp conductivity gradient. It may be optimal in creating a localized accumulation of charges which amplifies the geoelectric field together with ionospheric currents during the 2017 event. Also, if we look at the maximum absolute $\mathbf{E}_h$ values at MUO station during both events (7.1 V/km in 2003 and 6.8 V/km in 2017, Figure 4 (a),(b)), the station clearly has the highest values compared to all other stations.

Lastly, we experimented with different conductivity models effect on the simulated $\mathbf{E}_h$. We compared geoelectric fields calculated using 3D and 1D MT impedances. In 1D simulations, the Earth's crust is considered to have uniform electrical properties horizontally, and its properties change only in vertical direction. For each magnetometer location, we used corresponding 1D conductivity profiles from the 3D model of Fennoscandia to calculate local 1D MT impedances using a recursive formula for surface impedance (see, e.g., Trichtchenko and Boteler (2002) for more information). Results are shown in

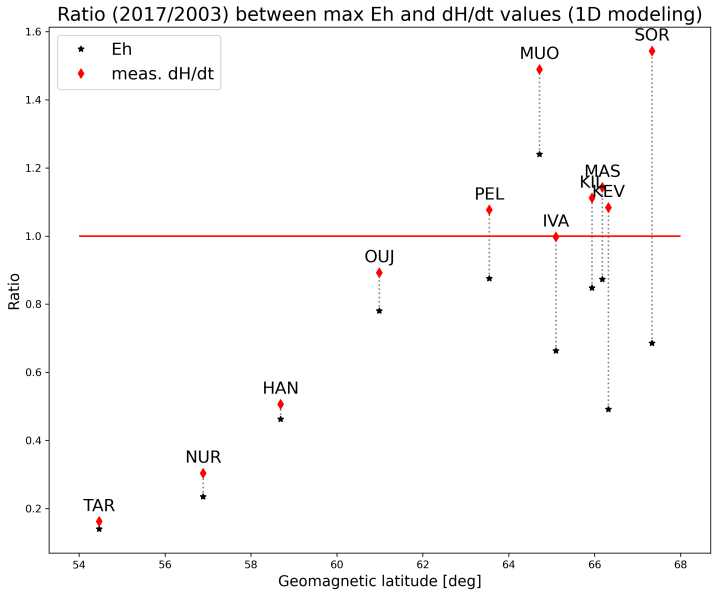

Figure 11. Same as Figure 3 but the geoelectric field modeling results are obtained using 1D MT impedances.

Figure 11. We found that there was no significant difference between ratios acquired using 3D and 1D MT impedances for considered locations. The largest difference was discovered for MUO station, which showed much larger $\mathbf{E}_h$ values for the 2017 event. This supports the hypothesis of significance of the ground conductivity gradient alongside with optimally oriented ionospheric currents. To summarize, we believe that the generally smaller $\mathbf{E}_h$ values at high latitudes are related to higher ground conductivity. MUO station is different because of the sharp conductivity gradient. We think that this is an interesting discovery and would like to analyse it more in future studies. Next we discuss the peaks in the normalized d$\mathbf{H}$/dt plots and use the 2D SECS plots of the external and internal currents to explain these peaks.

Strong external d$\mathbf{H}$/dt tend to occur when there is an intense ionospheric current that is abruptly modified (Juusola, Viljanen, Dimmock, et al., 2023). During the Halloween event d$\mathbf{H}$/dt peak (Figure 4 (c), at 20:08:30 UT), an intense, latitudinally extended westward electrojet (WEJ), disappeared. The d$\mathbf{J}_{eq}$/dt pattern (see Figure 6, left panel) describes the abrupt stopping of the WEJ current. During the 2017 storm, d$\mathbf{H}$/dt peak (23:50:40 UT), there is a localized d$\mathbf{J}_{eq}$/dt pattern caused by an eastward drifting channel of northward equivalent current.

The differences in the external d$\mathbf{H}$/dt at MUO during the 2003 and 2017 peaks were small, only a few nT/s (Figure 6). The most significant difference was in the internal d$\mathbf{H}$/dt, which was much stronger in the case of the 2017 event (Figure 7). The external d$\mathbf{J}_{eq}$/dt pattern over MUO was east-west oriented in the 2003 event and north-south oriented in the 2017 event (Figure 6). Clearly, the north-south orientation was optimal for inducing strong currents in the local north-south aligned conductivity structure (Figures 7,10). Thus, the reason why the 2017 event was stronger than the 2003 event at MUO was an intense time derivative of the external magnetic field that was optimally oriented to induce strong telluric currents in the local conductivity structure. The reason why intense d$\mathbf{H}$/dt disturbances were not observed at the lower latitude IMAGE stations in 2017, was that the ionospheric currents did not expand that far while in 2003 they did. Next we focus on the normalized $\mathbf{E}_h$ plots.

The 2003 $\mathbf{E}_h$ peak (19:54:40 UT) seems to be caused by a southward drifting WEJ (Figure 8). The peak occurs when the center of the WEJ passes the station. This approximately north-east to south-west oriented enhancement together with roughly parallel conductivity gradient seems to be optimal in creating strong $\mathbf{E}_h$. The 2017 $\mathbf{E}_h$ peak (Figure 4 (b), 23:17:50 UT) is caused by a southward drifting WEJ with a vortical $\mathrm{d}\mathbf{J}_{eq}/\mathrm{dt}$ pattern (Figure 8). The peak occurred when the center of the WEJ passed the station, i.e., the station was located approximately at the center of the $\mathrm{d}\mathbf{J}_{eq}/\mathrm{dt}$ vortex. The vortical $\mathrm{d}\mathbf{J}_{eq}/\mathrm{dt}$ pattern was caused by the drift: it describes how the WEJ current weakens at the northward flank of the WEJ and intensifies at the southward flank.

Both the external and internal $\mathrm{d}\mathbf{H}/\mathrm{dt}$ amplitudes were clearly weaker during the $\mathbf{E}_h$ peaks than during the $\mathrm{d}\mathbf{H}/\mathrm{dt}$ peaks (Figures 6-9). The north-east to south-west orientation of the $\mathrm{d}\mathbf{J}_{eq}/\mathrm{dt}$ together with the approximately parallel ground conductivity structure seems to enhance $\mathbf{E}_h$. Also, the vortical $\mathrm{d}\mathbf{J}_{eq}/\mathrm{dt}$ pattern that occurred during the 2017 $\mathbf{E}_h$ peak may be optimal for creating intense $\mathbf{E}_h$. This happens due to the intense $\mathrm{d}B_z/\mathrm{dt}$ at the center of the vortex that creates a strong induced divergence-free geoelectric field around it, for which $\mathrm{d}\mathbf{H}/\mathrm{dt}$ is a proxy (see Eq. 1). Such patterns also occur at substorm onsets (Juusola, Viljanen, Partamies, et al., 2023). To summarize our observations of the 2D SECS plot, we discovered that the ionospheric current structures were very different during the two magnetic storm. Still they caused geomagnetic and geoelectric disturbances of similar magnitude. This emphasizes the complicated interaction of the ionospheric currents and the ground conductivity. The ionospheric currents alone can not explain the localized peaks in the geoelectric field.

Another relevant study on the September 2017 storm was published by Wawrzaszek et al. (2023). They use IMAGE magnetometer data to calculate the geoelectric field with 1D ground conductivity models and utilize the GeoElectric Dynamic Mapping (GEDMap) to construct a spatial map of the geoelectric field. Their results on $\mathbf{E}_h$ modeling are in agreement with our study, despite some differences in the peak $\mathbf{E}_h$ time and magnitude. These differences are to be expected considering the different methods used. Next, we briefly describe the main sources of error in this study.

The main sources of error come from the SECS analysis and uncertainties in the geoelectric field modeling. The ground conductivity model used for the geoelectric field simulation is imperfect and could be improved, as stated by Kruglyakov et al. (2022). There is considerable uncertainty of the geoelectric field amplitudes, which can vary a lot in short (tens of kilometers) length scales (Marshalko et al., 2023). A possible way to circumvent this issue is to use relative values, i.e., comparison with respect to a benchmark event. We have used a ratio of the maximum $\mathbf{E}_h$ values (Figure 3), to minimize the effect of the uncertainty of the absolute values. However, assessing the amplitude uncertainty is difficult. This aspect is something to keep in mind when interpreting the results. For the purposes of our study, the timing of the $\mathbf{E}_h$ peaks is more relevant. Comparing with the study of Wawrzaszek et al. (2023), our modeled $\mathbf{E}_h$ time series look quite similar. Uncertainties associated with the SECS method are thoroughly discussed and deemed small in previous studies (Juusola et al. (2020), Kellinsalmi et al. (2022)).

Our study considered two major geomagnetic storms, but its results are not limited to these events. The ionospheric drivers are similar at equal geomagnetic latitudes (Juusola, Viljanen, Dimmock, et al., 2023). Balan et al. (2021) also found an UT-dependence of geomagnetic storms. So, our results can be extrapolated to apply for a wider set of space weather events. On the other hand, the geoelectric field depends strongly on the ground conductivity, leading to very different configurations at different regions even if the ionospheric sources are identical. Areas of sharp ground conductivity gradients (e.g. coastline) seem especially vulnerable to GIC, as also noted by Love et al. (2022) in the case of North-America. In Finland, the ground is also highly heterogeneous (Korja et al., 2002). This makes certain in-land areas more susceptible to geoelectric hazards. Overall, this gives an idea for further investigation of the variability of the geoelectric field

at a given location under the influence of different ionospheric drivers. One future research idea is to extend these results to a deeper analysis of a larger set of storms. For an end-user, such as a power grid operator, it could be quite useful to know how much larger or smaller a given event is compared to a benchmark. This can be figured out, for example, by comparing the maximum geoelectric field values. However, it may also be relevant to know whether there are only a few large geoelectric field spikes or more moderate but longer-term enhancement of the field, possibly leading to different impacts (see, e.g., Lewis et al. (2022); Reiter et al. (2021)). Another idea is to study the effects of location using one ionospheric driver and placing it at slightly different locations above the region under investigation. This way we could understand how much the geoelectric field varies at selected points when the location of the external source changes. This is a fundamental question of practical significance concerning GIC forecasts.

5 Conclusions

Our study compares two major geomagnetic storms caused by strong Earth-directed CMEs. This study reveals station-specific differences in the intensity of the magnetic field and geoelectric field variations. We observed localized magnetic and geoelectric field enhancements at high latitudes in the Fennoscandian region during the 2017 event, which exceeded (in the case of magnetic field time derivative) or were similar (in the case of the geoelectric field) to the values observed during the Halloween event. This is interesting because in general terms, e.g. magnetic indices, the Halloween event was clearly stronger.

The differences between the effects of these two storms at high latitudes are mostly explained by the ionospheric response to the CME arrival. For example, the location of the auroral oval and the abrupt changes in the ionospheric currents and vortical current structures can explain some of the local enhancements. Also the ground conductivity structure has a major impact on the local geomagnetic response, especially in the very heterogeneous structure in Finland. These findings help in explaining the localized peaks in $\mathrm{d}\mathbf{H}/\mathrm{dt}$ and $\mathbf{E}_h$. Our results give an estimate of other similar storm impacts on the geoelectric field and ultimately help to understand the very localized nature of GIC. These results also assist in understanding and making local risk assessments of induced currents. This study is yet another step towards better space weather preparedness.

6 Open Research

Data of geomagnetic field components and geomagnetic indices are from `http://space.fmi.fi/image/` and `https://wdc.kugi.kyoto-u.ac.jp/dstdir/`. Geomagnetic indices are available at `https://supermag.jhuapl.edu/indices`. The solar wind satellite observations are from the OMNIWeb service (King & Papitashvili, 2020). The SMAP model (Korja et al., 2002) is available at the European Plate Observing System (EPOS) portal via EPOS (2019) (stored in JSON format and compressed with bzip2) under CC BY-NC 4.0. PGIEM2G 3-D EM forward modeling code is developed openly at Gitlab and available at Kruglyakov (2022) under GPLv2. GIC data are available at the website of the Space and Earth Observation Centre of the Finnish Meteorological Institute (FMI) via FMI (2023) under CC BY 4.0.

Acknowledgments

We thank the institutes that maintain the IMAGE Magnetometer Array: Tromsø Geophysical Observatory of UiT the Arctic University of Norway (Norway), the Finnish Meteorological Institute (Finland), the Institute of Geophysics Polish Academy of Sciences (Poland), GFZ German Research Centre for Geosciences (Germany), the Geological Survey of Sweden (Sweden), the Swedish Institute of Space Physics (Sweden), Sodankylä Geophysical Observatory of the University of Oulu (Finland), Polar Geophysical Institute (Russia), and DTU Technical University of Denmark (Denmark). GIC recordings are maintained by the Finnish Meteorological Institute. We gratefully acknowledge the SuperMAG collaborators (https://supermag.jhuapl.edu/info/?page=acknowledgement). This research has been supported by the Academy of Finland (grant no. 339329).

References

Balan, N., Ram, S. T., Manu, V., Zhao, L., Xing, Z.-Y., & Zhang, Q.-H. (2021). Diurnal UT Variation of Low Latitude Geomagnetic Storms Using Six Indices. *Journal of Geophysical Research: Space Physics*, *126*(10), e2020JA028854. Retrieved 2023-11-15, from `https://onlinelibrary.wiley.com/doi/abs/10.1029/2020JA028854` (_eprint: https://agupubs.onlinelibrary.wiley.com/doi/pdf/10.1029/2020JA028854) doi: 10.1029/2020JA028854

Bedrosian, P. A., & Love, J. J. (2015). Mapping geoelectric fields during magnetic storms: Synthetic analysis of empirical United States impedances. *Geophysical Research Letters*, *42*(23), 10,160–10,170. Retrieved 2023-09-14, from `https://onlinelibrary.wiley.com/doi/abs/10.1002/2015GL066636` (_eprint: https://agupubs.onlinelibrary.wiley.com/doi/pdf/10.1002/2015GL066636) doi: 10.1002/2015GL066636

Berdichevsky, M. N., & Dmitriev, V. I. (2008). The Magnetotelluric Response Functions. In *Models and Methods of Magnetotellurics* (pp. 1–49). Berlin, Heidelberg: Springer Berlin Heidelberg. doi: 10.1007/978-3-540-77814-1_1

Blake, S. P., Pulkkinen, A., Schuck, P. W., Glocer, A., & Tóth, G. (2021). Estimating Maximum Extent of Auroral Equatorward Boundary Using Historical and Simulated Surface Magnetic Field Data. *Journal of Geophysical Research: Space Physics*, *126*(2), e2020JA028284. Retrieved 2023-05-03, from `https://onlinelibrary.wiley.com/doi/abs/10.1029/2020JA028284` (_eprint: https://agupubs.onlinelibrary.wiley.com/doi/pdf/10.1029/2020JA028284) doi: 10.1029/2020JA028284

Bolduc, L. (2002, November). GIC observations and studies in the Hydro-Québec power system. *Journal of Atmospheric and Solar-Terrestrial Physics*, *64*(16), 1793–1802. Retrieved 2023-09-14, from `https://www.sciencedirect.com/science/article/pii/S1364682602001281` doi: 10.1016/S1364-6826(02)00128-1

Boteler, D. H. (2013, April). A new versatile method for modelling geomagnetic induction in pipelines. *Geophysical Journal International*, *193*(1), 98–109. Retrieved 2023-09-14, from https://doi.org/10.1093/gji/ggs113 doi: 10.1093/gji/ggs113

Clilverd, M. A., Rodger, C. J., Brundell, J. B., Dalzell, M., Martin, I., Mac Manus, D. H., ... Obana, Y. (2018). Long-Lasting Geomagnetically Induced Currents and Harmonic Distortion Observed in New Zealand During the 7–8 September 2017 Disturbed Period. *Space Weather*, *16*(6), 704–717. Retrieved 2023-09-14, from https://onlinelibrary.wiley.com/doi/abs/10.1029/2018SW001822 (_eprint: https://agupubs.onlinelibrary.wiley.com/doi/pdf/10.1029/2018SW001822) doi: 10.1029/2018SW001822

Dimmock, A. P., Rosenqvist, L., Hall, J., Viljanen, A., Yordanova, E., Honkonen, I., ... Sjöberg, E. C. (2019, July). The GIC and Geomagnetic Response Over Fennoscandia to the 7–8 September 2017 Geomagnetic Storm. *Space Weather*, 2018SW002132. Retrieved 2021-02-10, from https://onlinelibrary.wiley.com/doi/abs/10.1029/2018SW002132 doi: 10.1029/2018SW002132

EPOS. (2019). *Dataset for "Crustal conductivity in Fennoscandia – a compilation of a database on crustal conductance in the Fennoscandian Shield", Korja et al., 2002, Earth, Planets and Space* [Dataset]. European Plate Observing System (EPOS). Retrieved from https://mt.research.ltu.se/MT/BEAR/1998/BEAR_3D.mod.json

FMI. (2023). *GIC recordings in the Finnish natural gas pipeline - ASCII files* [Dataset]. Finnish Meteorological Institute (FMI). Retrieved from https://space.fmi.fi/gic/man_ascii/man.php

Gao, J., Smirnov, M., Smirnova, M., & Egbert, G. (2021, March). 3-D time-domain electromagnetic modeling based on multi-resolution grid with application to geomagnetically induced currents. *Physics of the Earth and Planetary Interiors*, *312*, 106651. Retrieved 2023-09-14, from https://www.sciencedirect.com/science/article/pii/S0031920121000091 doi: 10.1016/j.pepi.2021.106651

Gjerloev, J. W. (2012). The supermag data processing technique. *J. Geophys. Res.*, *117*, A09213. doi: 10.1029/2012JA017683

Gopalswamy, N., Barbieri, L., Cliver, E. W., Lu, G., Plunkett, S. P., & Skoug, R. M. (2005). Introduction to violent Sun-Earth connection events of October–November 2003. *Journal of Geophysical Research: Space Physics*, *110*(A9). Retrieved 2023-09-14, from https://onlinelibrary.wiley.com/doi/abs/10.1029/2005JA011268 (_eprint: https://agupubs.onlinelibrary.wiley.com/doi/pdf/10.1029/2005JA011268) doi: 10.1029/2005JA011268

Hajra, R., Tsurutani, B. T., & Lakhina, G. S. (2020, August). The Complex Space Weather Events of 2017 September. *ApJ*, *899*(1), 3. Retrieved 2023-08-16, from https://dx.doi.org/10.3847/1538-4357/aba2c5 (Publisher: The American Astronomical Society) doi: 10.3847/1538-4357/aba2c5

Hapgood, M. (2019). The Great Storm of May 1921: An Exemplar of a Dangerous Space Weather Event. *Space Weather*, *17*(7), 950–975. Retrieved 2023-09-14, from https://onlinelibrary.wiley.com/doi/abs/10.1029/2019SW002195 (_eprint: https://agupubs.onlinelibrary.wiley.com/doi/pdf/10.1029/2019SW002195) doi: 10.1029/2019SW002195

IMAGE Magnetometer network [dataset]. (2023, May). Retrieved 2023-05-03, from https://space.fmi.fi/image/www/index.php?page=home

Juusola, L., Vanhamäki, H., Viljanen, A., & Smirnov, M. (2020, September). Induced currents due to 3D ground conductivity play a major role in the inter-

pretation of geomagnetic variations. *Ann. Geophys.*, *38*(5), 983–998. Retrieved 2021-02-10, from https://angeo.copernicus.org/articles/38/983/2020/ doi: 10.5194/angeo-38-983-2020

Juusola, L., Viljanen, A., Dimmock, A. P., Kellinsalmi, M., Schillings, A., & Weygand, J. M. (2023, January). Drivers of rapid geomagnetic variations at high latitudes. *Annales Geophysicae*, *41*(1), 13–37. Retrieved 2023-04-21, from https://angeo.copernicus.org/articles/41/13/2023/ (Publisher: Copernicus GmbH) doi: 10.5194/angeo-41-13-2023

Juusola, L., Viljanen, A., Partamies, N., Vanhamäki, H., Kellinsalmi, M., & Walker, S. (2023). Three principal components describe the spatiotemporal development of meso-scale ionospheric equivalent currents around substorm onsets. *EGUsphere*. Retrieved from https://doi.org/10.5194/egusphere-2023-1180 ([preprint])

Kappenman, J. G. (2005). An overview of the impulsive geomagnetic field disturbances and power grid impacts associated with the violent Sun-Earth connection events of 29–31 October 2003 and a comparative evaluation with other contemporary storms. *Space Weather*, *3*(8). Retrieved 2023-09-14, from https://onlinelibrary.wiley.com/doi/abs/10.1029/2004SW000128 (_eprint: https://agupubs.onlinelibrary.wiley.com/doi/pdf/10.1029/2004SW000128) doi: 10.1029/2004SW000128

Kelbert, A. (2020, January). The Role of Global/Regional Earth Conductivity Models in Natural Geomagnetic Hazard Mitigation. *Surv Geophys*, *41*(1), 115–166. Retrieved 2023-09-14, from https://doi.org/10.1007/s10712-019-09579-z doi: 10.1007/s10712-019-09579-z

Kellinsalmi, M., Viljanen, A., Juusola, L., & Käki, S. (2022, August). The time derivative of the geomagnetic field has a short memory. *Annales Geophysicae*, *40*(4), 545–562. Retrieved 2023-05-05, from https://angeo.copernicus.org/articles/40/545/2022/ (Publisher: Copernicus GmbH) doi: 10.5194/angeo-40-545-2022

King, J. H., & Papitashvili, N. E. (2020). *OMNI 5-min Data Set* [dataset]. NASA Space Physics Data Facility. Retrieved 2023-08-16, from https://hpde.io/NASA/NumericalData/OMNI/HighResolutionObservations/Version1/PT5M doi: 10.48322/GBPG-5R77

Korja, T., Engels, M., Zhamaletdinov, A. A., Kovtun, A. A., Palshin, N. A., Smirnov, M. Y., ... BEAR Working Group (2002, May). Crustal conductivity in Fennoscandia—a compilation of a database on crustal conductance in the Fennoscandian Shield. *Earth, Planets and Space*, *54*(5), 535–558. Retrieved 2023-09-14, from https://doi.org/10.1186/BF03353044 doi: 10.1186/BF03353044

Kruglyakov, M. (2022). *PGIEM2G* [Software]. Gitlab. Retrieved from https://gitlab.com/m.kruglyakov/PGIEM2G

Kruglyakov, M., Kuvshinov, A., & Marshalko, E. (2022). Real-Time 3-D Modeling of the Ground Electric Field Due To Space Weather Events. A Concept and Its Validation. *Space Weather*, *20*(4), e2021SW002906. Retrieved 2023-05-03, from https://onlinelibrary.wiley.com/doi/abs/10.1029/2021SW002906 (_eprint: https://agupubs.onlinelibrary.wiley.com/doi/pdf/10.1029/2021SW002906) doi: 10.1029/2021SW002906

Kruglyakov, M., Marshalko, E., Kuvshinov, A., Smirnov, M., & Viljanen, A. (2023). Multi-site transfer function approach for real-time modeling of the ground electric field induced by laterally-nonuniform ionospheric source. *Space Weather*, *21*(10), e2023SW003621. doi: https://doi.org/10.1029/2023SW003621

Kuvshinov, A., Grayver, A., Tøffner-Clausen, L., & Olsen, N. (2021). Probing 3-D electrical conductivity of the mantle using 6 years of Swarm, CryoSat-2 and

observatory magnetic data and exploiting matrix Q-responses approach. *Earth, Planets and Space*, *73*, 67. doi: 10.1186/s40623-020-01341-9

Lewis, Z. M., Wild, J. A., Allcock, M., & Walach, M.-T. (2022). Assessing the Impact of Weak and Moderate Geomagnetic Storms on UK Power Station Transformers. *Space Weather*, *20*(4), e2021SW003021. Retrieved 2023-09-14, from https://onlinelibrary.wiley.com/doi/abs/10.1029/2021SW003021 (_eprint: https://agupubs.onlinelibrary.wiley.com/doi/pdf/10.1029/2021SW003021) doi: 10.1029/2021SW003021

Love, J. J., Lucas, G. M., Rigler, E. J., Murphy, B. S., Kelbert, A., & Bedrosian, P. A. (2022). Mapping a Magnetic Superstorm: March 1989 Geoelectric Hazards and Impacts on United States Power Systems. *Space Weather*, *20*(5), e2021SW003030. Retrieved 2023-09-14, from https://onlinelibrary.wiley.com/doi/abs/10.1029/2021SW003030 (_eprint: https://agupubs.onlinelibrary.wiley.com/doi/pdf/10.1029/2021SW003030) doi: 10.1029/2021SW003030

Marshalko, E., Kruglyakov, M., Kuvshinov, A., Juusola, L., Kwagala, N. K., Sokolova, E., & Pilipenko, V. (2021). Comparing Three Approaches to the Inducing Source Setting for the Ground Electromagnetic Field Modeling due to Space Weather Events. *Space Weather*, *19*(2), e2020SW002657. Retrieved 2023-09-14, from https://onlinelibrary.wiley.com/doi/abs/10.1029/2020SW002657 (_eprint: https://agupubs.onlinelibrary.wiley.com/doi/pdf/10.1029/2020SW002657) doi: 10.1029/2020SW002657

Marshalko, E., Kruglyakov, M., Kuvshinov, A., & Viljanen, A. (2023). Three-Dimensional Modeling of the Ground Electric Field in Fennoscandia During the Halloween Geomagnetic Storm. *Space Weather*, *21*(9), e2022SW003370. Retrieved 2023-09-14, from https://onlinelibrary.wiley.com/doi/abs/10.1029/2022SW003370 (_eprint: https://agupubs.onlinelibrary.wiley.com/doi/pdf/10.1029/2022SW003370) doi: 10.1029/2022SW003370

Matzka, J., Bronkalla, O., Tornow, K., Elger, K., & Stolle, C. (2021). *Geomagnetic Kp index.* GFZ Data Services. Retrieved 2023-05-03, from https://dataservices.gfz-potsdam.de/panmetaworks/showshort.php?id=escidoc:5216888 doi: 10.5880/KP.0001

National risk assessment 2023 [Publication]. (2023, February). Retrieved 2023-10-18, from http://urn.fi/URN:ISBN:978-952-324-610-2 (Accepted: 2023-02-13T10:55:30Z, ISBN: 9789523246102)

Newell, P. T., & Gjerloev, J. W. (2011). Evaluation of supermag auroral electrojet indices as indicators of substorms and auroral power. *J. Geophys. Res.*, *116*, A12211. doi: 10.1029/2011JA016779

Phillips, D. t. (2021, October). *The Day Earth Lost Half Its Satellites (Halloween Storms 2003).* Retrieved 2023-10-11, from https://spaceweatherarchive.com/2021/10/28/the-day-earth-lost-half-its-satellites-halloween-storms-2003/

Pirjola, R. J., Boteler, D. H., Tuck, L., & Marsal, S. (2022, April). The Lehtinen–Pirjola method modified for efficient modelling of geomagnetically induced currents in multiple voltage levels of a power network. *Annales Geophysicae*, *40*(2), 205–215. Retrieved 2023-09-14, from https://angeo.copernicus.org/articles/40/205/2022/ (Publisher: Copernicus GmbH) doi: 10.5194/angeo-40-205-2022

Pulkkinen, A., Bernabeu, E., Thomson, A., Viljanen, A., Pirjola, R., Boteler, D., ... MacAlester, M. (2017, July). Geomagnetically induced currents: Science, engineering, and applications readiness: GIC Overview. *Space Weather*, *15*(7), 828–856. Retrieved 2021-02-10, from http://doi.wiley.com/10.1002/

2016SW001501 doi: 10.1002/2016SW001501

Pulkkinen, A., Lindahl, S., Viljanen, A., & Pirjola, R. (2005, August). Geomagnetic storm of 29-31 October 2003: Geomagnetically induced currents and their relation to problems in the Swedish high-voltage power transmission system: GEOMAGNETICALLY INDUCED CURRENTS. *Space Weather*, *3*(8), n/a–n/a. Retrieved 2021-02-10, from http://doi.wiley.com/10.1029/2004SW000123 doi: 10.1029/2004SW000123

Reiter, K., Guillon, S., Connors, M., & Jackel, B. (2021). Statistics of large impulsive magnetic events in the auroral zone. *J. Space Weather Space Clim.*, *11*, 44. Retrieved 2023-09-14, from https://www.swsc-journal.org/articles/swsc/abs/2021/01/swsc210007/swsc210007.html (Publisher: EDP Sciences) doi: 10.1051/swsc/2021029

Rosenqvist, L., Fristedt, T., Dimmock, A. P., Davidsson, P., Fridström, R., Hall, J. O., ... Wintoft, P. (2022). 3D Modeling of Geomagnetically Induced Currents in Sweden—Validation and Extreme Event Analysis. *Space Weather*, *20*(3), e2021SW002988. Retrieved 2023-09-14, from https://onlinelibrary.wiley.com/doi/abs/10.1029/2021SW002988 (_eprint: https://agupubs.onlinelibrary.wiley.com/doi/pdf/10.1029/2021SW002988) doi: 10.1029/2021SW002988

Schillings, A., Palin, L., Bower, G. E., Opgenoorth, H. J., Milan, S. E., Kauristie, K., ... Kamp, M. V. d. (2023). Signatures of wedgelets over Fennoscandia during the St Patrick's Day Storm 2015. *J. Space Weather Space Clim.*, *13*, 19. Retrieved 2023-09-14, from https://www.swsc-journal.org/articles/swsc/abs/2023/01/swsc220065/swsc220065.html (Publisher: EDP Sciences) doi: 10.1051/swsc/2023018

Schillings, A., Palin, L., Opgenoorth, H. J., Hamrin, M., Rosenqvist, L., Gjerloev, J. W., ... Barnes, R. (2022). Distribution and Occurrence Frequency of dB/dt Spikes During Magnetic Storms 1980–2020. *Space Weather*, *20*(5), e2021SW002953. Retrieved 2023-09-14, from https://onlinelibrary.wiley.com/doi/abs/10.1029/2021SW002953 (_eprint: https://agupubs.onlinelibrary.wiley.com/doi/pdf/10.1029/2021SW002953) doi: 10.1029/2021SW002953

Skoug, R. M., Gosling, J. T., Steinberg, J. T., McComas, D. J., Smith, C. W., Ness, N. F., ... Burlaga, L. F. (2004). Extremely high speed solar wind: 29–30 October 2003. *Journal of Geophysical Research: Space Physics*, *109*(A9). Retrieved 2023-03-03, from https://onlinelibrary.wiley.com/doi/abs/10.1029/2004JA010494 (_eprint: https://agupubs.onlinelibrary.wiley.com/doi/pdf/10.1029/2004JA010494) doi: 10.1029/2004JA010494

Trichtchenko, L., & Boteler, D. H. (2002). Modelling of geomagnetic induction in pipelines. *Annales Geophysicae*, *20*(7), 1063–1072. Retrieved from https://angeo.copernicus.org/articles/20/1063/2002/ doi: 10.5194/angeo-20-1063-2002

Tsurutani, Bruce T., & Hajra, Rajkumar. (2021). The Interplanetary and Magnetospheric causes of Geomagnetically Induced Currents (GICs) > 10 A in the Mäntsälä Finland Pipeline: 1999 through 2019. *J. Space Weather Space Clim.*, *11*, 23. Retrieved from https://doi.org/10.1051/swsc/2021001 doi: 10.1051/swsc/2021001

Vanhamäki, H., & Juusola, L. (2020). Introduction to Spherical Elementary Current Systems. In M. W. Dunlop & H. Lühr (Eds.), *Ionospheric Multi-Spacecraft Analysis Tools: Approaches for Deriving Ionospheric Parameters* (pp. 5–33). Cham: Springer International Publishing. Retrieved from https://doi.org/10.1007/978-3-030-26732-2_2 doi: 10.1007/978-3-030-26732-2_2

Wawrzaszek, A., Gil, A., Modzelewska, R., Tsurutani, B. T., & Wawrzaszek, R. (2023). Analysis of Large Geomagnetically Induced Currents Dur-

748 ing the 7–8 September 2017 Storm: Geoelectric Field Mapping. *Space*
749 *Weather*, *21*(3), e2022SW003383. Retrieved 2023-08-15, from `https://`
750 `onlinelibrary.wiley.com/doi/abs/10.1029/2022SW003383` (_eprint:
751 https://agupubs.onlinelibrary.wiley.com/doi/pdf/10.1029/2022SW003383) doi:
752 10.1029/2022SW003383
753 Xiong, C., Lühr, H., Wang, H., & Johnsen, M. G. (2014, June). Determining
754 the boundaries of the auroral oval from CHAMP field-aligned current sig-
755 natures – Part 1. *Annales Geophysicae*, *32*(6), 609–622. Retrieved
756 2023-04-27, from `https://angeo.copernicus.org/articles/32/609/`
757 `2014/angeo-32-609-2014.html` (Publisher: Copernicus GmbH) doi:
758 10.5194/angeo-32-609-2014
759 Zou, Y., Dowell, C., Ferdousi, B., Lyons, L. R., & Liu, J. (2022). Auroral
760 drivers of large dB/dt during geomagnetic storms. *Space Weather*, *20*(11),
761 e2022SW003121. Retrieved from `https://agupubs.onlinelibrary.wiley`
762 `.com/doi/abs/10.1029/2022SW003121` (e2022SW003121 2022SW003121) doi:
763 https://doi.org/10.1029/2022SW003121